Dual-probe 1D hybrid fs/ps rotational CARS for simultaneous single-shot temperature, pressure, and O2/N2 measurements

Dual-probe 1-d hybrid fs/ps rotational CARS for simultaneous single-shot temperature, pressure, and O_2/N_2 measurements

DAVID ESCOFET-MARTIN[1,*], ANTHONY O. OJO[1], JOSHUA COLLINS[1], NILS TORGE MECKER[1], MARK LINNE[1], AND BRIAN PETERSON[1]

[1] Institute for Multiscale Thermofluids, University of Edinburgh, Edinburgh, UK.
[*] Corresponding author: david.escofet@ed.ac.uk

Compiled June 18, 2020

We employ dual-probe 1-d fs/ps hybrid rotational coherent anti-Stokes Raman spectroscopy to investigate simultaneous temperature, pressure, and O_2/N_2 measurements for gas-phase diagnostics. The dual-probe HRCARS technique allows for simultaneous measurements from the time and frequency-domain. A novel approach for measuring pressure, which offers high accuracy (<1%) and precision (0.42%) is presented. The technique is first demonstrated in a chamber for a range of pressures (1-1.5 bar). This technique shows an impressive capability of resolving 1-d pressure gradients arising from a N_2 jet impinging on a surface, both in laminar and turbulent conditions. The technique is shown to be capable of resolving single-shot pressure gradients (0.04 bar/mm) originating from kinetic energy conversion to pressure, and resolves characteristic O_2/N_2 structures from laminar and turbulent mixing.

http://dx.doi.org/10.1364/ao.XX.XXXXXX

Temperature is a key thermodynamic variable in reactive flows, because chemical reaction rates are exponentially temperature dependent. Spatially-resolved pressure relates to molecular motion and forces, and it is critical for aerodynamic studies. Relative species concentrations are essential when evaluating turbulent mixing [1] prevalent in many practical applications where two gases have to be combined. There is thus a need for spatially-resolved, 1-d gas-phase measurements of pressure, temperature and species; which would support flow simulations and optimize operation of system components in practical devices such as jet engines and gas turbines.

Laser techniques for pressure and temperature are non-intrusive [2]. In gas-phase thermometry, coherent anti-Stokes Raman spectroscopy (CARS) is esteemed for measurement precision and accuracy [3]. Historically, nanosecond (ns) CARS provided 0-d temperature measurements through highly resolved spectra [4], and simultaneous temperature and pressure measurements were performed by utilizing different spectral features in the frequency-domain [5, 6].

New technological developments such as high energy picosecond (ps) and femtosecond (fs) lasers have granted the extension of CARS measurements from 0-d to 1-d [7], and to 2-d [8]. This technological developments permitted time-domain experiments to resolve collisional behavior. Fs and ps time-resolved CARS has been used to infer Raman coherence decay information [9, 10] and temperature [11, 12].

Encoding time-domain information into the frequency-domain has been done by chirped-probe-pulse (CPP) CARS [13] but remains complex and limited to 0-d. Recently, Prince et al [14] introduced hybrid fs/ps CARS (HCARS), this technique employs fs beams for the pump/Stokes and a ps beam for the probe. With fs/ps HCARS frequency-domain information is time-resolved due to the narrow probe, while time-domain information can be obtained by scanning the probe delay. The significance of this new configuration can be observed in measurements applied in a wide range of pressures, temperatures, and species [15–21]. Frequency-domain temperature sensitivity is maximized when using short delays compared to coherence dephasing timescales.

Multiple-probe HCARS experiments, have been demonstrated in 0-d to correct temperature for time-varying collisional environments [22]. The frequency-domain pressure dependence of HCARS has been exploited to measure pressure [23]. Using this pressure dependence and multiple probes, simultaneous pressure and temperature measurements were performed in 0-d [24] and 1-d [25]. Single-shot temporally and spectrally-resolved information has been recently demonstrated in 0-d [26], although limitations in laser energy and detector dimensionality complicate spatially-resolved measurements.

This paper introduces dual-probe 1-d hybrid fs/ps rotational CARS for simultaneous single-shot temperature, pressure, and O_2/N_2 ratio measurements. This analysis exploits the strong time-domain pressure dependence of the CARS signal for accurate and precise pressure measurements.

The HRCARS technique is demonstrated here in two environments. The first is an optically accessible chamber [27] to

evaluate the accuracy of the pressure measurements. The second is a high speed N_2 jet impinging on a surface, to demonstrate the utility of the technique in capturing 1-d pressure gradients.

Figure 1 illustrates the experimental setup for the N_2 impinging jet tests and it is similar to that used for the chamber tests. The setup is modified from previous 1-d HRCARS experimental layouts [7] to include two probe beams. The seed (Vitara(slave)) of a Ti:Sapphire amplifier delivering 35 fs pulses with 7.5 mJ at 1 kHz is locked to the 9^{th} harmonic of the master oscillator frequency (80 MHz) of a diode pumped Nd:Yag providing 20 ps pulses with 20 mJ at 50 Hz. The locking is achieved through the synchrolock to allow for a small jitter (< 1 ps) between the two pulses.

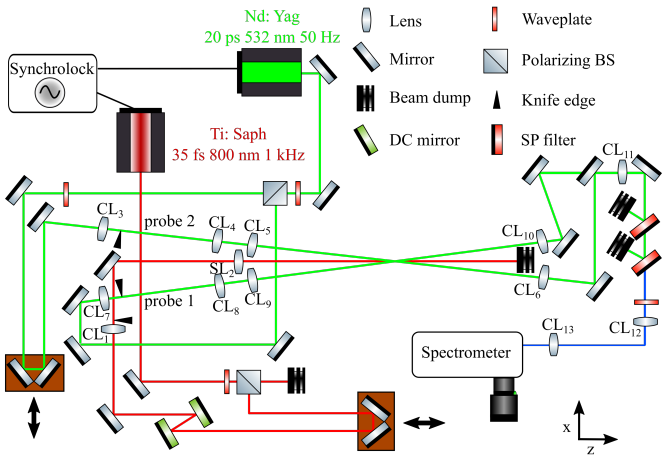

Fig. 1. Schematic of the experimental setup for the N_2 impinging jet measurements.

The pump/Stokes energy is adjusted using a variable attenuator (waveplate + polarizing beam splitter (BS)). We use dispersion compensation (DC) mirrors to precompensate for dispersion effects caused by the lenses CL_1 and SL_2. A total compensation of -220 fs^2 provides a near Fourier-transformed pulse after going through the lenses. A combination of a cylindrical lens (CL_1, f_1=300 mm) and a spherical lens (SL_2, f_2=300mm) create a laser sheet that intersects the probe beam sheet. The probe beam is split (with a waveplate + polarizing BS) into 2 probes: 5% to probe 1 ($\tau_1 \approx 40\ ps$) and 95% to probe 2 ($\tau_2 \approx 270\ ps$). Two translation stages are used to control the relative delays between the three beams. Two pairs of cylindrical lenses ($CL_{3,4}$, $f_{3,4}$=150mm & $CL_{7,8}$, $f_{7,8}$=150 mm), with the optical power aligned with the y axis and separated by 2f are placed in the optical path. The cylindrical lenses $CL_{4,8}$ image a knife-edge into the probe volume with a magnification slightly < 1. The knife-edge prevents scattering of the beam from the impinging surface. Lenses $CL_{5,9}$ ($f_{5,9}$=250 mm) with the optical power along the x-axis, create two laser sheets. The laser sheets cross at the probe volume with an angle of 5° with the pump/Stokes. This allows for similar phase matching for both probes. The beams are then collimated with $CL_{6,10}$ ($f_{6,10}$=400 mm). The mirrors placed between the probe volume and CL_{11} are positioned such that both path lengths are the same. The probe volume (0.055 x 1.2 x 4.5 mm^3, Δx x Δz x Δy) is relay imaged into the entrance of the spectrometer using lenses CL_{11} and CL_{12} (f_{11}=500 mm, f_{12}=250 mm). The anti-Stokes and Stokes signals are separated using two angle-tunable short-pass (SP) filters. A cylindrical lens CL_{13} (f_{13}=100 mm) focuses the light into the spectrometer. The 0.75 m spectrometer is equipped with a 2400 gr/mm grating, which disperses the HRCARS signal onto an EMCCD. The dispersion is 0.18 cm^{-1}/pixel with a spectral resolution of 0.75 cm^{-1} (FWHM). The magnification of the lens pair $CL_{7,8}$ and CL_{11} is set to ≈0.8. The EMCCD is binned 2x1 in the y-direction and is operated at 25 Hz with 1 ms exposure for a spatial to pixel relationship of 30 μm/pixel. Figure 2(a) shows a representative single-shot spectrogram of the CARS intensity, where the two probes are imaged one on top of the other. The resolution of the imaging system is 60 μm, found by evaluating the sharpness of the imaged knife-edge. A total length of ≈ 4.5 mm (≈ 30 μm/pixel, 150 pixels) is evaluated from the surface. 1-d HRCARS spectrograms are corrected for the finite bandwith of the pump/Stokes pulses by scanning the probe beam delay with respect to the pump/Stokes in an argon environment. A weighted average from these delays is used to correct the experimental spectrograms. This cross-correlation is also used to define the 0 ps delay in the model.

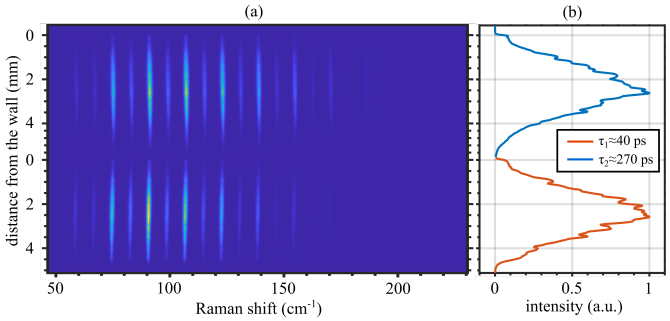

Fig. 2. (a) Single-shot spatially and temporally-resolved spectrogram of the dual-probe fs/ps HRCARS near the symmetry axis for the laminar N_2 impinging jet. (374x1024 pixels) (b) Single-shot spatially and temporally-resolved projected intensity of the dual-probe fs/ps HRCARS.

For the chamber experiments, the aforementioned knife-edges (Fig.1) together with the lenses $CL_{1,3,4,7,8}$ are removed and SL_2 is substituted for a cylindrical lens with f=300 mm. Due to the increased dispersion from the chamber windows (12 mm fused silica), the number of bounces between the DC mirrors is increased to provide -440 fs^2. The measured pulse after passing through the window is 37 fs (FWHM). The energy employed for the pump/Stokes beam is significantly reduced (<3 mJ) due to supercontinuum light generation in the chamber windows.

The CARS model used here is detailed in [28, 29]. Pressure dependent linewidths are included with self-broadened linewidths for N_2 [21] and O_2-N_2 for O_2 [30]. For the frequency-domain fitting, due to the need to fit about 15000 spectra for a single measurement (100 shots x 150 rows), a 3-dimensional library with varying temperature, pressure and O_2/N_2 ratio was employed.

The spatially-resolved intensities for different probe delays shown in Fig. 2(b) are key to studying the time-domain pressure fitting. The intensity from integrating the frequency-domain CARS signal is

$$I_{CARS}(T,P,\tau) \propto \int \mathcal{F}\left[P^{(3)}(t,\tau,T,P)\right] d\omega \qquad \textbf{(1)}$$

where $P^{(3)}$ is the third order polarization

$$P^{(3)}(t,\tau,T,P) \propto \left(\frac{i}{\hbar}\right) E_{pr}(t-\tau) R_{CARS}(t,T,P) e^{i\omega_{pr}(t-\tau)}. \qquad \textbf{(2)}$$

E_{pr} is the normalized electric field envelope of the probe, τ is the relative delay between the probe and the pump/Stokes, and R_{CARS} is the molecular response function

$$R_{CARS}(t,T,P) = \frac{P}{kT}\sum_{J} I_{J;J+2}(T) \times e^{\frac{t}{\hbar}\left(i\Delta E_{J;J+2} - \frac{1}{2}\Gamma_{J;J+2}(T,P)\right)}, \quad \textbf{(3)}$$

where P/kT represents the number density effect, $I_{J;J+2}$ is the Raman transition strength, $\Delta E_{J;J+2}$ is the frequency of the transitions, and $\Gamma_{J;J+2}$ the linewidths.

Given electric fields for pump/Stokes and probe, the N_2 HRCARS intensity is a function of probe delay, temperature and pressure (Eq.1-3). Figure 3(a) shows the simulated I_{CARS} for two probe delays ($\tau_1 \approx 40$ ps, $\tau_2 \approx 270$ ps) and the I_{ratio}=$I_{CARS\tau1}/I_{CARS\tau2}$ for a range of pressures 0.9-1.1 bar and temperatures 280-310 K. The Raman response ($R_{CARS}(t,T,P)$) contains two pressure dependent terms: number density (P/kT) and linewidths ($\Gamma_{J;J+2}(T,P)$). For probe 1 ($I_{CARS\tau1}$, $\tau_1 \approx 40$ ps), the number density contribution dominates the signal intensity for both decreasing temperature and increasing pressure. For probe 2 ($I_{CARS\tau2}$, $\tau_2 \approx 270$ ps) the signal decreases for increasing pressure due to the exponential dependence on linewidth, which overcomes the quadratic signal increase due to number density.

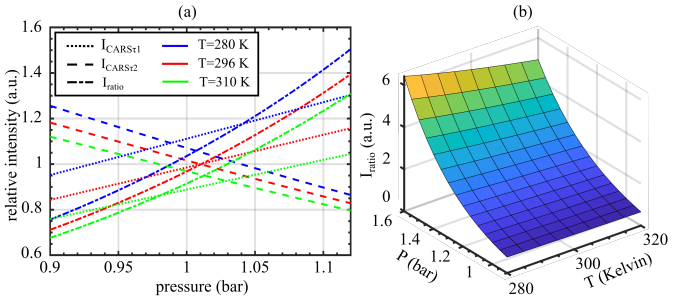

Fig. 3. (a) Simulated intensity as a function of pressure (0.9-1.1 bar) and temperature (280-310 K) for early probe ($\tau_1 \approx 40$ ps), late probe ($\tau_2 \approx 270$ ps) and I_{ratio}(b) Simulated relation for I_{ratio}, pressure and temperature.

The I_{ratio} for spatially correlated measurements is not a function of number density nor laser energy, and the pressure sensitivity is increased when compared to any of the individual probes. The relation between the simulated I_{ratio} and the measured I_{ratio} is not complete until a calibration measurement is performed. This accounts for the energy profiles of both individual probe beams, among other things, and is performed separately for chamber and jet experiments, both at ambient pressure and temperature. To better utilize the detector dynamic range, the energy split of probes 1 and 2 is adjusted so that $I_{ratio} \approx 1$ under the calibration conditions.

Figure 3(b) shows the simulated normalized I_{ratio} for a range of temperatures 280-310 K and pressures 0.9-1.6 bar. The surface plot illustrates the strong sensitivity of the I_{ratio} with respect to pressure; a variation from 1 to 1.6 bar produces an I_{ratio} change bigger than 5 for this temperature range. The I_{ratio} sensitivity with respect to pressure is predominantly a function of $\Delta\tau = \tau_2 - \tau_1$ and can be adjusted to match the expected measured pressure to the dynamic range of the detector.

The fitting procedure starts by assuming ambient pressure in a frequency-domain fit to probe 1, so we obtain temperature ($T_{1_{st}}$). This temperature is then used to obtain pressure using the I_{ratio}-pressure relation. The calculated pressure is then used to refit probe 1 resulting in the final temperature (T). With the final temperature and the I_{ratio}-pressure relation we can obtain the final pressure (P) that has already converged. The statistics displayed in table 1 are for spatially and time-resolved measurements in the chamber, from evaluating the central 20 spectral rows in 50 shots. The spatio-temporal measurement precision is hindered compared to the N_2 impinging jet experiments due to the reduced pump/Stokes energy (<3 mJ).

Table 1. Pressure and temperature measurements in the chamber

$\overline{T_{1_{st}}}$(K)	$\overline{T}$(K)	$\overline{P}$(bar)	$\frac{\sigma_T}{\overline{T}}$ (%)	$\frac{\sigma_P}{\overline{P}}$ (%)	$\overline{P_{trans.}}$(bar)
296.43	296.43	1.01	1.36	0.83	1.01
298.59	296.59	1.22	1.14	1.29	1.21
299.73	296.87	1.31	1.08	1.72	1.30
300.17	296.64	1.38	1.04	1.91	1.37
301.30	296.83	1.48	0.94	2.44	1.49

$T_{1_{st}}$ shows a systematic increase of 1.7% as pressure increases 0.47 bar, while the final calculated temperature ($\overline{T}$) only varies 0.2% in the studied pressure range. The pressure measurements are benchmarked against a pressure transducer ($\overline{P_{trans.}}$). The agreement between $\overline{P}$ with $\overline{P_{trans.}}$ is better than 1 %. The temperature precision improves from 1.36 to 0.94% as pressure increases, due to the increased signal from $I_{CARS\tau1}$. The pressure precision decreases from 0.83 to 2.44% as pressure increases, due to the signal decrease from $I_{CARS\tau2}$.

To demonstrate the utility of the dual-probe HRCARS technique, measurements were applied to a N_2 jet impinging on a surface. The surface is slightly curved along the z-direction (d=300 mm) for easier optical access. Measurements are performed under two conditions, $\overline{V}$=3.8 m/s (Re=1160, laminar) and $\overline{V}$=76 m/s (Re=23230, turbulent). The jet inner diameter is D=4.5 mm and the distance between the jet and the surface is H=11 mm; providing a non-dimensional H/D ratio of 2.44. The 4.5 mm closest to the plate are evaluated for temperature, pressure, and O_2/N_2. For every 2-d field, 20 1-d measurements are performed, spaced every 200 μm covering the radial direction $\pm$2 mm of the jet impingement. The surface covered is (4 x 4.5 mm^2, Δx x Δy), each averaged field contains the analysis of (150 x 20 x 100) 0.3 million spectra.

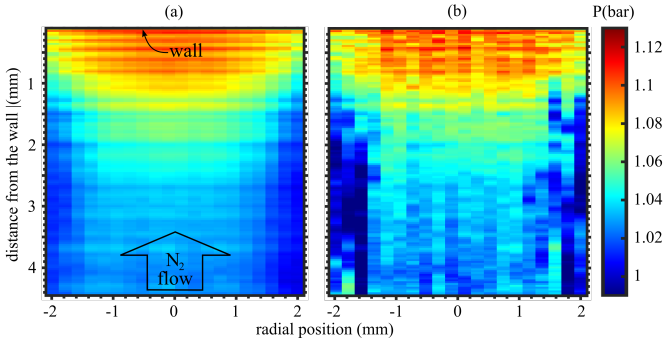

Fig. 4. 2-d pressure field from a turbulent (Re=23230) N_2 jet impinging on a surface: (a) averaged and (b) single-shot.

The laminar pressure field, and the laminar and turbulent

temperature fields are uniform (ambient), thus not shown here. The pressure and temperature fields obtained from the laminar jet, are used to evaluate the measurement precision. The spatio-temporal precision for pressure is 0.42% ($\sigma_P/\overline{P}$) and for temperature is 0.62% ($\sigma_T/\overline{T}$). Figures 4(a) and (b) show averaged and instantaneous turbulent pressure fields respectively. The maximum measured pressure is ≈1.11 bar in both the averaged and single-shot fields. This maximum pressure is located near the symmetry axis close to the surface and decays both radially and axially. From the pressure measurements, spatial pressure gradients of the order of 0.04 bar/mm are well-captured.

To further illustrate the jet behavior, Figure 5 shows both averaged and single-shot O_2/N_2 ratios for both the laminar (a), (b) and the turbulent conditions (c), (d). The stagnating flow field causes no O_2 detection close to the plate. Comparing both O_2/N_2 averaged fields, the turbulent field has O_2/N_2 ≈0.06 ratio, a three-fold increase due to enhanced air entrainment near the jet radius. The mixing mechanisms are captured in the single-shot measurements: for the laminar conditions, the O_2/N_2 measurements show smooth O_2/N_2 gradients typical of mixing dominated mostly by diffusion, compared to the fine structure of air pockets for the turbulent case that demonstrates the exceptional spatial resolution.

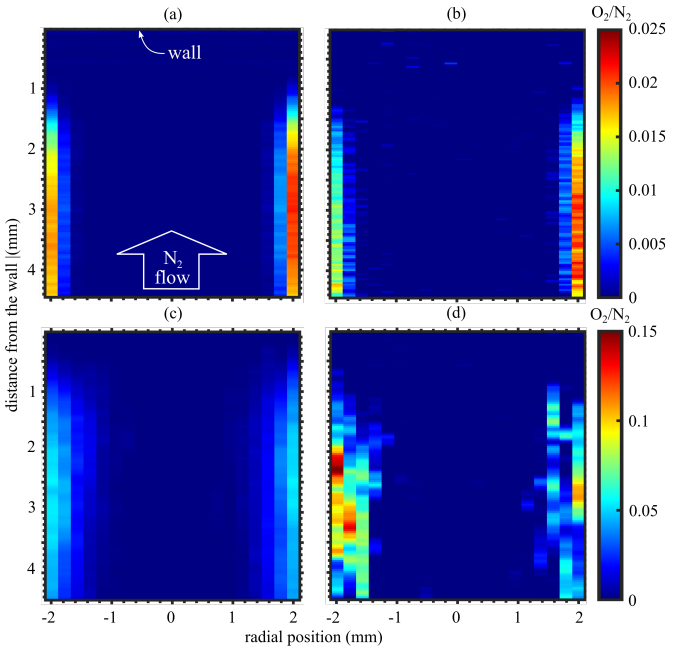

Fig. 5. 2-d O_2/N_2 field from a N_2 jet impinging on a surface: laminar jet ((a) averaged field, (b) single shot field) and turbulent jet ((c) averaged field, (d) single shot field).

In summary, with dual-probe 1-d HRCARS, by extracting information from both the time and frequency-domains, we have demonstrated simultaneous pressure, temperature, and O_2/N_2 ratio measurements. A new methodology to evaluate pressure leads to high accuracy (<1%) for the pressure range 1-1.5 bar; remarkable spatio-temporal temperature precision of 0.62% ($\sigma_T/\overline{T}$), unmatched spatio-temporal pressure precision of 0.42% ($\sigma_P/\overline{P}$); and fine spatial resolution (0.055 x 1.2 x 0.060 mm^3). The pressure measurements are able to describe spatial pressure gradients of the order of 0.04 bar/mm, that arise from kinetic energy conversion to pressure, due to a high speed jet impinging on a surface. The measurements also capture the spatial characteristics from the mixing interface both in laminar and turbulent conditions. Applying this measurement technique in a more challenging environment with sharp pressure, temperature, and species gradients, will be the focus of future work.

Funding. European Research Council (ERC grant #759546) and EPSRC (EP/P020593/1, EP/P001661/1).

Disclosures. The authors declare no conflicts of interest.

REFERENCES

1. P. E. Dimotakis, Annu. Rev. Fluid Mech. **37**, 329 (2005).
2. A. Y. Chang, B. E. Battles, and R. K. Hanson, Opt. Lett. **15**, 706 (1990).
3. S. Roy, J. R. Gord, and A. K. Patnaik, Prog. Energy Combust. Sci. **36**, 280 (2010).
4. F. Beyrau, T. Seeger, A. Malarski, and A. Leipertz, J. Raman Spectrosc. **34**, 946 (2003).
5. R. E. Foglesong, S. M. Green, R. P. Lucht, and J. C. Dutton, AIAA J. **36**, 234 (1998).
6. R. L. Farrow, R. Trebino, and R. E. Palmer, Appl. Opt. **26**, 331 (1987).
7. A. Bohlin, B. D. Patterson, and C. J. Kliewer, J. Chem. Phys. **138** (2013).
8. A. Bohlin and C. J. Kliewer, J. Chem. Phys. **138** (2013).
9. G. Knopp, P. Beaud, P. Radi, M. Tulej, B. Bougie, D. Cannavo, and T. Gerber, J. Raman Spectrosc. **33**, 861 (2002).
10. V. Morozov, S. Mochalov, A. Olenin, V. Tunkin, and A. Kouzov, J. Raman Spectrosc. **34**, 983 (2003).
11. S. Roy, P. J. Kinnius, R. P. Lucht, and J. R. Gord, Opt. Commun. (2008).
12. T. Seeger, J. Kiefer, A. Leipertz, B. D. Patterson, C. J. Kliewer, and T. B. Settersten, Opt. Lett. **34**, 3755 (2009).
13. D. R. Richardson, R. P. Lucht, W. D. Kulatilaka, S. Roy, and J. R. Gord, Appl. Phys. B: Lasers Opt. **104**, 699 (2011).
14. B. D. Prince, A. Chakraborty, B. M. Prince, and H. U. Stauffer, J. Chem. Phys. **125** (2006).
15. J. D. Miller, M. N. Slipchenko, T. R. Meyer, H. U. Stauffer, and J. R. Gord, **35**, 2430 (2010).
16. N. Torge Mecker, T. L. Courtney, B. D. Patterson, D. Escofet-Martin, B. Peterson, C. J. Kliewer, and M. Linne, J. Opt. Soc. Am. B **37**, 1035 (2020).
17. J. D. Miller, C. E. Dedic, and T. R. Meyer, J. Raman Spectrosc. **46**, 702 (2015).
18. A. Bohlin, E. Nordström, B. D. Patterson, P. E. Bengtsson, and C. J. Kliewer, J. Chem. Phys. **137** (2012).
19. J. D. Miller, S. Roy, J. R. Gord, and T. R. Meyer, J. Chem. Phys. **135** (2011).
20. W. D. Kulatilaka, P. S. Hsu, H. U. Stauffer, J. R. Gord, and S. Roy, Appl. Phys. Lett. **97**, 1 (2010).
21. C. J. Kliewer, A. Bohlin, E. Nordström, B. D. Patterson, P. E. Bengtsson, and T. B. Settersten, Appl. Phys. B: Lasers Opt. **108**, 419 (2012).
22. B. D. Patterson, Y. Gao, T. Seeger, and C. J. Kliewer, Opt. Lett. **38**, 4566 (2013).
23. S. P. Kearney and P. M. Danehy, Opt. Lett. **40**, 4082 (2015).
24. C. E. Dedic, A. D. Cutler, and P. M. Danehy, AIAA Scitech 2019 Forum (2019).
25. S. P. Kearney, D. R. Richardson, J. E. Retter, C. E. Dedic, and P. M. Danehy, AIAA Scitech 2020 Forum (2020).
26. A. Hosseinnia, M. Ruchkina, P. Ding, P.-E. Bengtsson, and J. Bood, Opt. Lett. **45**, 308 (2020).
27. D. Escofet-Martin, A. O. Ojo, N. T. Mecker, M. A. Linne, and B. Peterson, Proc. Combust. Inst. p. submitted for publication (2021).
28. C. Yang, D. Escofet-Martin, D. Dunn-Rankin, Y. C. Chien, X. Yu, and S. Mukamel, J. Raman Spectrosc. **48**, 1881 (2017).
29. C. Yang, P. He, D. Escofet-Martin, J.-B. Peng, R.-W. Fan, X. Yu, and D. Dunn-Rankin, Appl. Opt. **57**, 197 (2018).
30. G. Millot, R. Saint-Loup, J. Santos, R. Chaux, H. Berger, and J. Bonamy, The J. Chem. Phys. **96**, 961 (1992).